Towards a Field-Ready HF-VHF Ground-Based Ice Penetrating Synthetic Aperture Radar: Forward Modelling and Validation for SAR Imaging

J. D. Hawkins*[1], L. B. Lok[1], P. V. Brennan[1], K. W. Nicholls[2]
[1]Radar Group, Department of Electronic & Electrical Engineering, UCL, UK
[2]British Antarctic Survey, Cambridge, UK
*Corresponding Author: jonathan.hawkins.17@ucl.ac.uk

***Abstract*— A ray-based 2D modelling approach is proposed to reduce computation times involved in the forward-modelling of deramped frequency-modulated continuous wave (FMCW) radar signals for subglacial ice features. The model generation procedure and link-budget are described, prior to validation and benchmarking of the ray-based approach using a commercial 3D FDTD simulator. The proposed model results in a reduced computation time of three orders of magnitude per range profile, for comparable power and phase outputs. This provides a highly efficient numerical method for investigating subglacial ice structures with more realistic sizes and features.**

***Keywords*— ice-penetrating radar, SAR, forward modelling**

I. Introduction

Current approaches to studying the subglacial ice-ocean interface using satellite [1], airborne [2] and ground-based ice penetrating radar surveys [3] are all limited by operational constraints that prevent the study the ice shelf base in sufficient resolution in space and time. CryoSat-2 has an annual ground-track repeat cycle and ice shelf thickness estimates are limited to a 1 km cross-track resolution, which exceeds observed widths of some subglacial channels [2]. Ground-based seismic, airborne and ground-based radar surveys can measure ice-shelf topography with finer cross-track resolutions (at metre scales) than remote sensing methods, however are limited to summer months because of the requirement for human operators.

Ground-based synthetic aperture radar (SAR) has the potential to meet the demand for monitoring the temporal evolution of basal features on ice shelves. The Autonomous phase-sensitive Radio Echo Sounder (ApRES) has been successfully deployed in the polar regions to measure basal melt rates on ice shelves [4]. To increase the practical spatial coverage of a survey, at the cost of reduced vertical resolution, a reduced frequency ApRES is in development with a centre frequency of 30 MHz for use with an autonomous rover to collect ground-based SAR data. Validation of the SAR processing workflow prior to data collection requires synthetically generated radar profiles for relevant ice shelf geometries.

Synthetic radar data generated using forward modelling is widely exploited to help interpret the results of surveys in terms of the possible presence of englacial and subglacial structures [5]–[7]. 3D electromagnetic modelling for glacial or ice-shelf scale structures in the order of hundreds of metres can result in large simulation times [8], encouraging development of finite-difference tools for glacial and planetary radar sounding [9] which truncate the simulation domain to 2D.

After defining three representative subglacial geometries in Section II, this paper describes a 2D ray-tracing forward-modelling approach for efficiently generating synthetic ApRES SAR data in Section III. The ray-tracing model is validated against simulation results from a commercial 3D electromagnetic solver in Section IV. The paper concludes in Section V with discussion of ongoing work.

II. Synthetic Subglacial Models

Three subglacial topographies were chosen to validate the forward modelling approach (Fig. 1): the step model represents a moderate (1:4) slope in the basal interface; the terrace model represents multiple short step changes in basal elevation [10] and the channel model represents a subglacial hydrological channel upstream of the grounding line [3]. The latter two models were selected from evidence available in glaciological and oceanographic literature, while the first model mimics the basal terrace geometry with a reduced slope angle and on a shorter spatial scale. Each model domain is constant in the y direction.

The set of materials considered in each of the models is summarised in Table 1 and all materials are initially considered to be lossless and homogenous. The large difference in permittivity, and hence propagation velocity, between ice and water results in small mesh steps for gridded computational electromagnetics (CEM) techniques or excessive memory

Table 1. Dielectric properties for materials in Fig. 1, repeated from [11]. Permittivity and loss tangent for subglacial till is derived using the Looyenga mixing equation for unfrozen bedrock with a 33% concentration of freshwater.

Domain	Material	$\varepsilon_\mathbf{r}$	$\tan\delta$
Proglacial	Air	1	-
Englacial	Ice	3.2	0.001
	Freshwater	80	0.002
Subglacial	Seawater	77	11.3
	Unfrozen Bedrock	6.6	0.41
	Subglacial Till	20	3.66

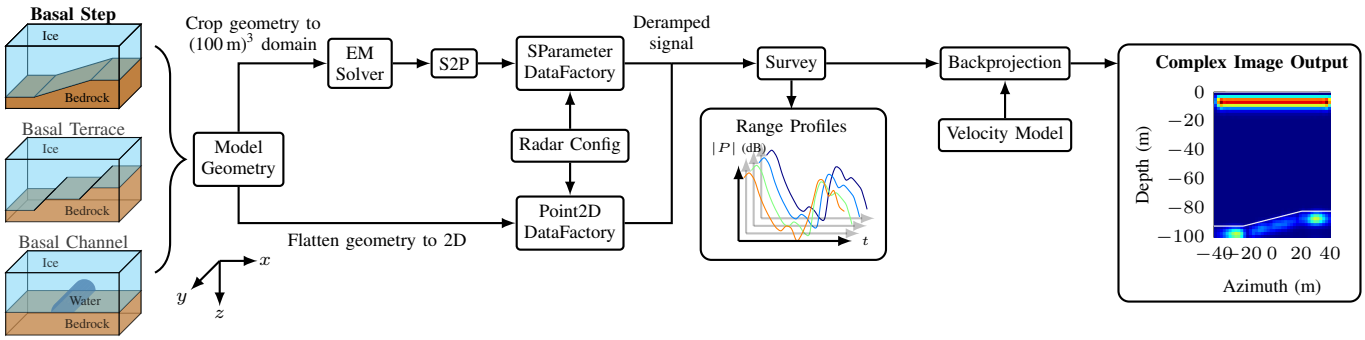

Fig. 1. Workflows for ray-based 2D and commercial 3D EM simulations of basal-geometry showing the intermediate range-profiles and final SAR image.

requirements for the method of moments (MoM). The subglacial materials in this paper are restricted to unfrozen bedrock and subglacial till to minimise the computational requirements of CEM models. Hence in this development phase, seawater in the basal step and terrace geometries is (temporarily) replaced with bedrock.

III. Ray-based 2D Forward Modelling

The ray-based forward modelling approach is implemented in MATLAB® 2020 and exploits the two-dimensional symmetry in the proposed models. The modelling problem is defined by a vertical stack of M+1 dielectric layers that extend infinitely in the x-y plane and defined by M piecewise linear interfaces in the x-z plane. Point scatterers are defined at a fixed spatial interval along each dielectric interface from which a point-scatterer FMCW response is summed to generate the time-domain deramped signal. The deramped signal for a point-scatterer in an FMCW radar is taken from [4] to be

$$d(t,\tau) = \cos\left(\omega_c\tau + K\tau(t - T/2) - K\tau^2/2 + \phi_0\right) \quad (1)$$

where ω_c is the center angular frequency, τ is the two-way travel time (TWTT) of the received chirp, ϕ_0 is an initial offset phase, and K is the angular sweep rate $2\pi B/T$ for a radar bandwith of B and chirp duration of T. The TWTT is determined for each discretised point-target on the dielectric interface for each survey location, as defined by a set of (x, z) coordinates. A radar configuration object specifies the FMCW chirp parameters (ω_c, B, T), transmit power and antenna parameters which impact the link budget.

Each interface is defined as a set of N_m coordinate pairs (x, z) where m is the interface index. These pairs are linearly interpolated such that each line segment is split into further sub-segments as in Fig. 2, with a maximum length L (in metres) which is calculated as

$$L = \mathrm{PSF} \cdot \lambda_c / \sqrt{\max\left(\varepsilon_m, \varepsilon_{m+1}\right)} \quad (2)$$

where λ_c is the center-wavelength in free space and PSF is a point-scaling factor to allow for fine-tuning of segment length (set to 0.25 by default). If an integer number of segments of length L cannot be used in the interpolation between points (x_i, z_i) and (x_{i+1}, z_{i+1}) then the PSF is reduced. To enable the simulation of rough surfaces - more representative of realistic subglacial topography - an additional variance argument σ_m can be provided to each interface which adds a normally distributed random offset in the z direction (to prevent the introduction of occluded scatterers). The resultant deramped signal for a single radar position is therefore given by Huygen's principle as

$$d(t) = \sum_{m=0}^{M} \sum_{i=0}^{I_m} d(t, \tau_{i,m}) \sqrt{P_T Z_0 G_{i,m} / I_m} \quad (3)$$

where I_m is the number of discretised segments on the m^{th} interface, P_T is the transmitted power, Z_0 is the reference impedance and $G_{i,m}$ is the link budget for the i^{th} segment on the m^{th} interface. The travel-time $\tau_{i,m}$ is given by the sum $\tau_{i,m} = \tau_1 + \tau_2 + \ldots + \tau_{2m+2}$, where the propagation velocity through each layer is determined by $c_0/\sqrt{\varepsilon_m}$ and hence the intersection point on each intermediate interface is found by minimising $\tau_{i,m}$ (in accordance with Fermat's principle).

A. Link Budget

The link budget for each layer segment $G_{i,m}$ is written

$$G_{i,m} = G_{ant} G_\Gamma G_{sca} G_{AF} G_{sys} / A_d \quad (4)$$

where G_{ant} is the total transmit and receive antenna gain (including the effect of directivity), G_Γ combines accumulated transmission losses and segment reflectivity, A_d

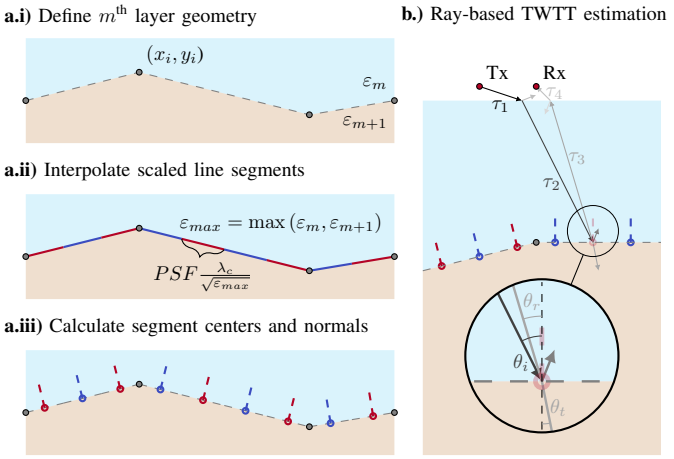

Fig. 2. **a.)** Layer discretisation process from (x, z) coordinate pairs to piecewise segment centers and normal vectors. **b.)** Ray-based travel time estimation for reflection at dielectric interface.

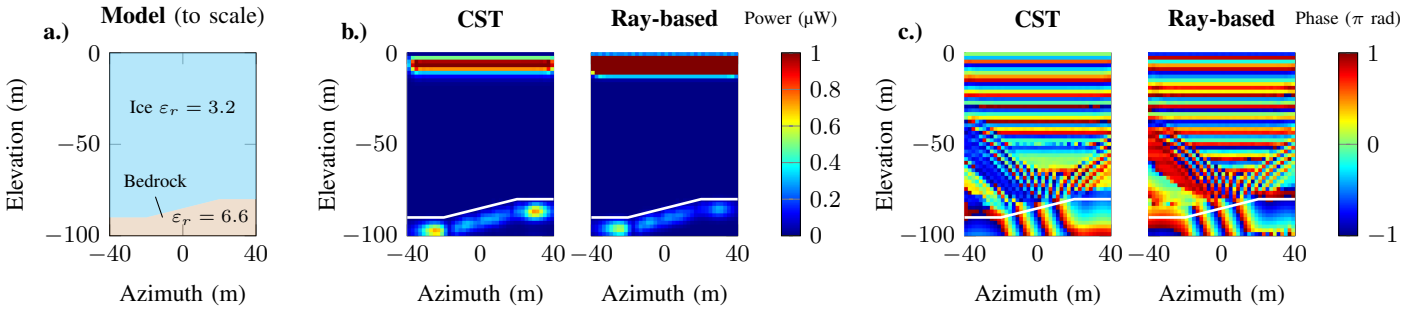

Fig. 3. **a.)** Model geometry and comparison of backprojected images generated using the synthetic ray-based 2D model and validation 3D data using SIMULIA CST Studio 2020. Both sets of results are generated from 161 radar profiles from –40 m to 40 m in steps of 0.5 m. Images are backprojected on a 2m×2m grid and show **b.)** power referenced to 50 Ω and **c.)** phase, with ground-truth geometry of the basal interface in white for each image. The antennas are positioned 0.1 m above the surface in a background permittivity of $\varepsilon_r = 1$ and separated by 10 m. Ray-based power results are normalised by a factor of 10^{-3}.

is the round-trip dielectric attenuation through each layer, G_{sca} accounts for geometric scattering, G_{AF} refers to the frequency-dependent deramped filter gain and G_{sys} refers to additional system gain effects.

The transmit and receive antenna gains are each specified as a singular value or an angle-dependent (θ) directivity function. Assuming perfect radiation efficiency, this is combined with either a monochromatic or frequency-dependent S_{11} to calculate the combined power gain for both antennas as

$$[G_{ant}]_{\mathrm{dB}} = [G_{\mathrm{Tx}}(\omega,\theta)]_{\mathrm{dB}} + [G_{\mathrm{Rx}}(\omega,\theta)]_{\mathrm{dB}} \tag{5}$$

The materials in this paper are all assumed to be lossless, however the ray-based modelling approach has the capability to implement dielectric attenuation in the form

$$[A_d]_{\mathrm{dB}} = (\mathbf{r}_{\mathrm{Tx}} + \mathbf{r}_{\mathrm{Rx}})\mathbf{a}^{\intercal} \text{ (dB/meter)} \tag{6}$$

where for the m^{th} layer, $\mathbf{a}$ is a (1×m+1) vector of dielectric attenuation for each layer and $\mathbf{r}_{\mathrm{Tx}}$, $\mathbf{r}_{\mathrm{Rx}}$ are the (1×m+1) vectors of distances travelled through each layer for the transmit and receive ray respectively.

The reflection coefficient $|\Gamma_m|^2$ of the m^{th} interface is calculated using Fresnel's formulae for either perpendicular or parallel polarisations [12] where the *H*-plane is assumed parallel to the y-z plane and the *E*-plane is parallel to the x-z plane. If there are intermediate interfaces between the radar and the m^{th} interface then the signal is attenuated by the intermediate Fresnel transmission coefficients to maintain conservation of energy which is written as

$$T_m = \sum_{k=0}^{m-1}(1 - |\Gamma_k|^2) \tag{7}$$

The reflectivity depends on both θ_i and θ_b known as the bidirectional reflectance distribution function (BDRF) of the interface. The BDRF of the interface results from the integrated response across each illuminated scattering center (dependent on the value of PSF and an optional random offset) in a similar manner to the radiation pattern of a phased antenna array. With each scattering center being representative of a planar segment of the dielectric interface (extending in the y axis), a local BDRF relative to the segment normal is introduced. To account for variation in arrival angle and small-scale roughness an empirical 'glossy' BDRF is defined as

$$\mathrm{BDRF}(\theta_i,\theta_r)^{\frac{1}{s}} = \cos(\theta_i)\cos(\theta_r)\left[1+\cos(\theta_i+\theta_r)\right]/2 \tag{8}$$

where θ_i and θ_r are the incident and reflected angles with respect to the segment normal, and s is a specularity coefficient ($s > 0$). Internal horizons within glacial ice are often specular while the ice-bedrock response is usually diffusive [13], and hence either an experimentally derived BDRF or modified specularity coefficient can be defined for each interface. Thus, G_Γ is given as

$$G_\Gamma = |\Gamma_m|^2 T_m \mathrm{BDRF}(\theta_i,\theta_r) \tag{9}$$

Each scatterer has a radar cross section (RCS) approximated by a rectangular plane segment with length $L_{i,m}$ (in the x-z plane) and a width determined by the resolution (ΔR) limited footprint of the radar at range R given by $\sqrt{2R\Delta R}$. Thus the scattering loss is determined by accounting for the geometric spreading of incident and re-radiated energy from each segment as

$$G_{sca} = \frac{\lambda_0^2 L_{i,m}\sqrt{(||\mathbf{r}_{\mathrm{Tx}}|| + ||\mathbf{r}_{\mathrm{Rx}}||\Delta R)}}{8\pi^3||\mathbf{r}_{\mathrm{Tx}}||^2||\mathbf{r}_{\mathrm{Rx}}||^2} \tag{10}$$

The radar configuration describes parameters (and nominal values) listed in Table 2 which affect the modelled received signal power, contribute to G_{sys} and introduce non-linearities in the received signal through the deramped filter gain G_{AF} and emulated ADC quantisation and thermal noise.

IV. EM Validation

SIMULIA CST Studio 2020 was used as the 3D-CEM tool to verify and benchmark the ray-based 2D model results. Extending the Finite Difference Time Domain (FDTD) simulation domain to the length of the model geometry would result in excessive simulation times, particularly in the terrace and channel models. Instead, models of the HF ApRES wire-mesh antennas [14] are positioned in the centre of the x-y plane and the basal geometry is shifted along the x axis of a fixed simulation domain with dimensions of 100 m in each cardinal direction. Data acquisition mimics that of a stepped frequency radar with antennas orientated with the dipole axis in the x-axis.

Table 2. List of radar configuration parameters and nominal values.

Radar Parameter	Symbol	Nom. Value	Unit/Data Type
Transmit Power	P_t	0.1	W
Centre Frequency	ω_c	30	MHz
Bandwidth	B	20	MHz
Chirp Period	T	1	s
Sampling Frequency	f_s	40	kHz
Range Resolution (in ice)	ΔR	4.19	m
Noise Figure	F	4	(-)
Ambient Temperature	T_A	298	K
ADC Bit Depth	N_{ADC}	16	bits
ADC Voltage Range	V_{ADC}	2.5	V
Tx Antenna Offset	δ_{Tx}	(0,0,0)	3x1 ENU Vector
Rx Antenna Offset	δ_{Rx}	(0,0,0)	3x1 ENU Vector
Cable Propagation Factor	v_{cable}	1	(-)
Deramp Gain Function	$H_D(\omega)$	1	(-)
LNA Gain	G_{LNA}	1	(-)
RF Input Attenuation	G_{RFin}	1	(-)

A model dimension of 100 m is chosen which exceeds the resolution limited footprint of 57.9 m for a geometry with a maximum depth of 100 m beneath the antenna. An *H*-field symmetry in the *E*-plane of the antennas was invoked and the resultant model yielded approximately 100 million meshcells which could be simulated in less than 1 hour per range profile with a high end computing cluster. Two-port *s*-parameters were bandlimited to 20 to 40 MHz over 501 discrete frequency points and exported for each radar position (which corresponds to the x-axis shift introduced into the model geometry). The real part of the complex *s*-parameter data is used as the deramped signal in the processing workflow (Fig. 1).

A. Backprojection

A time-domain backprojection algorithm is used to form SAR images on the x-z plane from the simulated range profiles. The backprojection routine in Fig. 3 uses a constant velocity model, which yields reasonable results for the three-layer basal step model under consideration but may introduce errors by not accounting for the effect of refraction at the surface. The ray-based simulations introduce an additional shift in TWTT as they include an offset to account for the effect of propagation along the cable from the radar system, positioned between both antennas. Fig. 3 shows that the backprojected images exhibit similar spatial scattering behaviour in both magnitude and phase response along the basal step, however further work is required to normalise the ray-based magnitude response to provide comparable output magnitudes. Table 3 compares compute timings for the generation of the range profiles and backprojected images. The 2D ray-based method is three orders of magnitude faster in generating range profiles for comparable imaging performance.

V. Conclusion

Initial results from a 2D ray-based forward modelling approach for SAR processing of synthetic HF-VHF ApRES radar datasets are shown to yield comparable results to full-3D electromagnetic models with a thousand-fold increase in computation speed. Various features of the ray-based model are presented to introduce real-world non-linearities and behaviour that may affect the resultant SAR image. Future work will involve validation of the remaining subglacial models and the introduction of changes in model geometry over multiple surveys to develop a workflow for spatio-temporal analysis of basal melt on ice shelves.

Table 3. Comparison of computation times for CST 3D and ray-based 2D simulations of the basal step model.

Simulator	Operation	$\max \varepsilon_{\mathbf{r}}$	Platform	Time (s) (per profile)
CST 3D	Range Profle	6.6	HEC	1081
		20	HEC	3379
3x Nvidia GV100 32 GB GPUs	Backproj.	6.6	Desktop	0.11
		20	Desktop	0.10
Ray-based 2D	Range Profle	6.6	Desktop	1.34
		20	Desktop	2.37
1x i7-7700HQ 20 GB RAM	Backproj.	6.6	Desktop	0.10
		20	Desktop	0.12

Acknowledgment

This work is supported by the Royal Society Research Fellows Enhancement Award RGF\EA\180173.

References

[1] S. J. Chuter and J. L. Bamber, "Antarctic ice shelf thickness from CryoSat-2 radar altimetry," *Geophys. Res. Letts.*, vol. 42, no. 24, pp. 10,710–721,729, dec 2015.

[2] A. M. Le Brocq *et al.*, "Evidence from ice shelves for channelized meltwater flow beneath the Antarctic Ice Sheet," *Nature Geoscience*, vol. 6, no. 11, pp. 945–948, 2013.

[3] R. Drews *et al.*, "Actively evolving subglacial conduits and eskers initiate ice shelf channels at an Antarctic grounding line," *Nature Comms.*, vol. 8, no. May, 2017.

[4] P. V. Brennan *et al.*, "Phase-sensitive FMCW radar system for high-precision Antarctic ice shelf profile monitoring," *IET Radar, Sonar & Navigation*, vol. 8, no. 7, pp. 776–786, 2014.

[5] O. Eisen *et al.*, "Revealing the nature of radar reflections in ice: DEP-based FDTD forward modeling," *Geophys. Res. Letts.*, vol. 30, no. 5, pp. 1–4, 2003.

[6] G. Church *et al.*, "Monitoring the seasonal changes of an englacial conduit network using repeated ground-penetrating radar measurements," *The Cryosphere*, vol. 14, no. 10, pp. 3269–3286, 2020.

[7] T. R. Hillebrand *et al.*, "Radio-echo sounding and waveform modeling reveal abundant marine ice in former rifts and basal crevasses within Crary Ice Rise, Antarctica," *J. Glac.*, pp. 1–12, 2021.

[8] L. Langhammer *et al.*, "Ground-penetrating radar antenna orientation effects on temperate mountain glaciers," *Geophysics*, vol. 82, no. 3, pp. H15–H24, 2017.

[9] Y. Lei *et al.*, "A 2-d pseudospectral time-domain (pstd) simulator for large-scale electromagnetic scattering and radar sounding applications," *IEEE Transactions on Geoscience and Remote Sensing*, vol. 58, no. 6, pp. 4076–4098, 2020.

[10] P. Dutrieux *et al.*, "Basal terraces on melting ice shelves," *Geophys. Res. Letts.*, vol. 41, no. 15, pp. 5506–5513, aug 2014.

[11] M. E. Peters, D. D. Blankenship, and D. L. Morse, "Analysis techniques for coherent airborne radar sounding: Application to West Antarctic ice streams," *J. Geophys. Res. Solid Earth*, vol. 110, no. B6, p. B06303, jun 2005.

[12] C. A. Balanis, *Advanced engineering electromagnetics*, 2nd ed. Hoboken, N.J.: Hoboken, N.J. : Wiley, 2012.

[13] N. Holschuh, K. Christianson, and S. Anandakrishnan, "Power loss in dipping internal reflectors, imaged using ice-penetrating radar," *Ann. Glaciol.*, vol. 55, no. 67, pp. 49–56, 2014.

[14] J. D. Hawkins *et al.*, "HF Wire-Mesh Dipole Antennas for Broadband Ice-Penetrating Radar," *IEEE Antennas Wirel. Propag. Lett.*, vol. 19, no. 12, pp. 2172–2176, 2020.